Fabrication of micro-structured surface with controllable randomness by using FTS-based diamond turning

Shigeru Tanikawa, Jiwang Yan [*]

Department of Mechanical Engineering, Faculty of Science and Technology, Keio University, 3-14-1 Hiyoshi, Kohoku-ku, Yokohama, 223-8522, Japan

A B S T R A C T

Random micro-structured surfaces (RSS) have great application potentials as various functional surface elements, such as optical diffusers, with homogeneous surface properties. Conventional fabrication methods for RSS, such as chemical etching, can no longer meet modern requirements of high precision and controllability. In this study, a novel method was proposed for fabricating micro dimple arrays with controllable randomness in dimple size and depth by using fast tool servo (FTS)-based single-point diamond turning. Firstly, for tool path generation, a computer program was developed to periodically arrange small patches of quadratic surfaces over a large surface area. Then the position, height, and size of each quadratic surface were adjusted by applying random values, whose dynamic range was preset, to control the spatial difference among the dimples. Finally, the designed RSS was machined by continuous and segment cutting methods, respectively, to evaluate their effects on dimple edge formation. Results showed that the segmented cutting method improved the edge accuracy, thus was effective for RSS machining. The machined surface matched precisely with the designed surface with a form error of 10 nm level. The machining method proposed in this study enables high-precision patterning of mold inserts for molding/imprinting RSS on polymer materials.

1. Introduction

There are many potential applications of a random micro-structure surface (RSS) in the industry. The unique features of RSS make it a useful surface with a wide range of applications to realize nondirectional and homogeneous surface properties. For examples, owing to its characteristics of large surface area and random reflection, RSS is used in anti-slip and matting technologies [1,2]. Products that utilize RSS with improved interfacial performances are widely used in our daily lives [3]. It has been reported that RSS shows high hydrophobicity or hydrophilicity due to its random surface micro-structures [4–6].

In addition, RSS is widely used as an important optical element [7]. When an incident light is transmitted through an RSS made of glass or polymer, the light is refracted by the random surface structures of the RSS and is scattered into random directions to avoid directional nonuniformity. There are many different types of RSS for light diffusion [8–10]. Among these RSS diffusers, especially, a randomized microlens array makes it possible to achieve highly homogenized light diffusion while controlling the intensity profile of incident light [11–14]. Thus, the microlens array RSS has been used as illumination elements in optoelectronic devices such as smartphones, displays, and projectors [11,15,16].

Moreover, RSS diffusers are used in 3D sensing technology [7,16]. The 3D sensing technology using the time-of-flight method can measure the depth of an object based on the time difference between the reflection of the irradiated diffuse light on the object and the detection of the reflected light by the detector [17]. The broad light diffusion allows for the expansion of the measurement range, and the homogenized light diffusion promotes the improvement of the measurement accuracy. As can be seen from these examples, the demand of RSS diffuser is growing rapidly. In some recent applications, precise control of the randomness of the size and depth of the surface microstructure of RSS is required.

To meet the increasing demand for the RSS-based devices, it is necessary to develop new manufacturing methods for mass production of high-quality RSS optical elements. An RSS is conventionally fabricated by dry/wet etching [18–21]. The non-directional nature of material dissolution and removal in chemical etching enables generation of random surface structures. While etching has the advantage of enabling mass production of large-area RSS, it is difficult to precisely control and predict the surface structure shape and its randomness. In addition, the

etching processes need masks, and usually employ some poisonous chemicals as reactants, which pose a public health and environmental risk.

To solve these problems, fabrication of RSS by using fast tool servo (FTS)-based single-point diamond turning might be an effective and eco-friendly approach. Diamond turning enables numerically controlled ultra-precision machining of complicated surfaces designed by computer programs [22–24]. Especially, FTS-based diamond turning, which realizes high-speed tool motions with high positioning accuracy, can improve the working efficiency without scarifying machining fidelity and surface integrity [25–27]. Due to these advantages, FTS-based diamond turning has been extensively explored and applied to various fields, including fabricating freeform optics and micro-structured functional surfaces [24,25].

In this study, novel methods were proposed for designing and fabricating RSS with controllable randomness by using FTS-based single-point diamond turning. A design method of RSS with controllable randomness was introduced, and the effect of each parameter used in the RSS design were discussed. Then, tool paths were generated based on the designed RSS, and dimple arrays with random sizes and depths were generated by FTS-based diamond turning. The proposed methods were proved to enable flexible control of the randomness of surface structure, and in turn, contribute to high-efficiency and high-precision machining of ideal RSS for optical applications.

2. Theory and method

2.1. Light diffusion by RSS

The light diffusion in a microlens array RSS is shown in Fig. 1. The diffused light is obtained by refracting the incident light through each microlens with randomness. The randomness causes the focal point to shift, which realizes highly homogenized light diffusion [12–14]. In addition, microlens array RSS can control the light diffusion by the depth and size of each lens, which can be also used for beam shaping [11,13,14]. Diffusion angle is an important factor in determining the performance of an optical diffuser. The diffusion angle θ is calculated from the following equation [28]:

$$\theta = 2 \, tan^{-1}\left(\frac{r}{l}\right) \tag{1}$$

where r is the distance from the center of the diffused light and l is the spacing between the diffuser and the screen, respectively. In order to precisely adjust the diffusion angle, accurate control of the randomness of microlens size/depth is required.

2.2. RSS design method

In this study, the targeted RSS is composed of multiple microlens dimples with quadratic surfaces of random size and depth, which can be

expressed as:

$$z = \frac{2E \cdot d}{w^2}\left\{A(x-B)^2 + C(y-D)^2\right\} - E \cdot d \tag{2}$$

where x, y, z are coordinate variables, A, B, C, D, and E are shape parameters for controlling the size, the position along X- and Y-axes, and the depth of a dimple, respectively; d and w are the depth and width of the basic dimple, as shown in Fig. 2. By generating random numbers for the shape parameters, each dimple had a different quadratic surface, as shown in Fig. 3. These randomized quadratic surfaces show that the size, position, and depth can be flexibly adjusted by the parameters.

Each randomized quadratic surface was arranged in a grid by the following equation to determine the center point (c_x, c_y) :

$$c_{x,i} = \frac{w}{2}(2i - N_x - 1) \quad (i = 1, 2, \cdots\cdots, N_x) \tag{3-a}$$

$$c_{y,j} = \frac{w}{2}(2j - N_y - 1) \quad (j = 1, 2, \cdots\cdots, N_y) \tag{3-b}$$

where i, j, N_x, and N_y are the number of each and all quadratic surface along X- and Y- direction, respectively. A designed RSS formed by these arranged dimples is defined by selecting and combining the smallest overlapping value in the Z-axis direction by utilizing the mesh grid. The point cloud data used in the mesh grid was generated according to the following equation:

$$x_m = \left(\frac{N_x w}{M_x - 1}\right)(s - 1) - \frac{N_x w}{2} \quad (s = 1, 2, \cdots\cdots, M_x) \tag{4-a}$$

$$y_m = \left(\frac{N_y w}{M_y - 1}\right)(t - 1) - \frac{N_y w}{2} \quad (t = 1, 2, \cdots\cdots, M_y) \tag{4-b}$$

where M_x and M_y are the number of meshes in the X- and Y-axes, s and t are an integer value between 1 and M_x or M_y, respectively. Each quadratic surface represented by these point cloud data was continuously connected by using the following equation to select the minimum value:

The case $z_{1,1}(x_m(s), y_m(t)) < z_{i,j}(x_m(s), y_m(t)) \rightarrow z_{1,1}(x_m(s), y_m(t))$
$$= z_{1,1}(x_m(s), y_m(t)) \tag{5-a}$$

The case $z_{1,1}(x_m(s), y_m(t)) > z_{i,j}(x_m(s), y_m(t)) \rightarrow z_{1,1}(x_m(s), y_m(t))$
$$= z_{i,j}(x_m(s), y_m(t)) \tag{5-b}$$

where $z_{i,j}$ are functions representing the i-th and j-th quadratic surface from the X- and Y- axes, $x_m(s)$ and $y_m(t)$ are functions indicating the point cloud coordinates of the mesh grid along the X- and Y-axes, respectively, as shown in Fig. 4. The values of i, j, s, and t were increased in turn, and the values of the reference point cloud data at $z_{1,1}$ were overwritten one after another according to the above conditional expression. Finally, by inverting all calculated point cloud data of $z_{1,1}$, the RSS was completed.
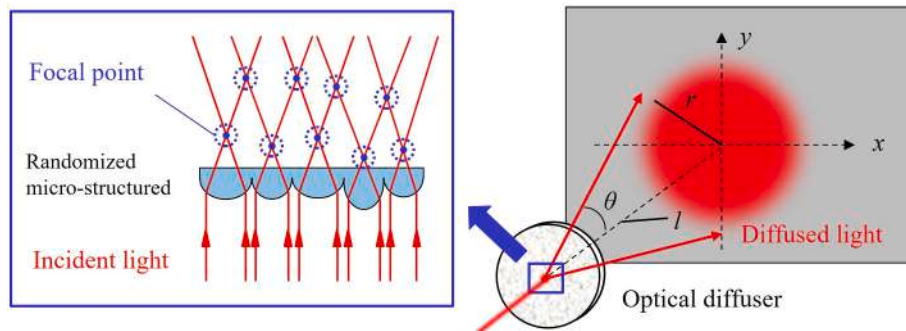

Fig. 1. Schematic of light diffusion by microlens array RSS.
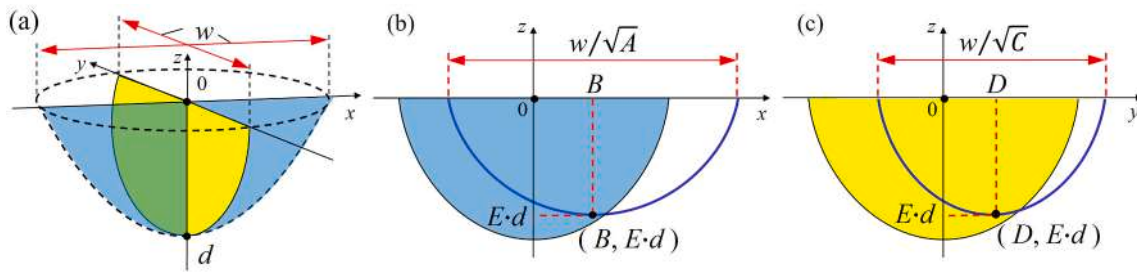
Fig. 2. Diagram showing the relationship between each variable and shape of a quadratic surface: (a) 3D view, (b) Z-Y, and (c) Z-X cross-sectional views.
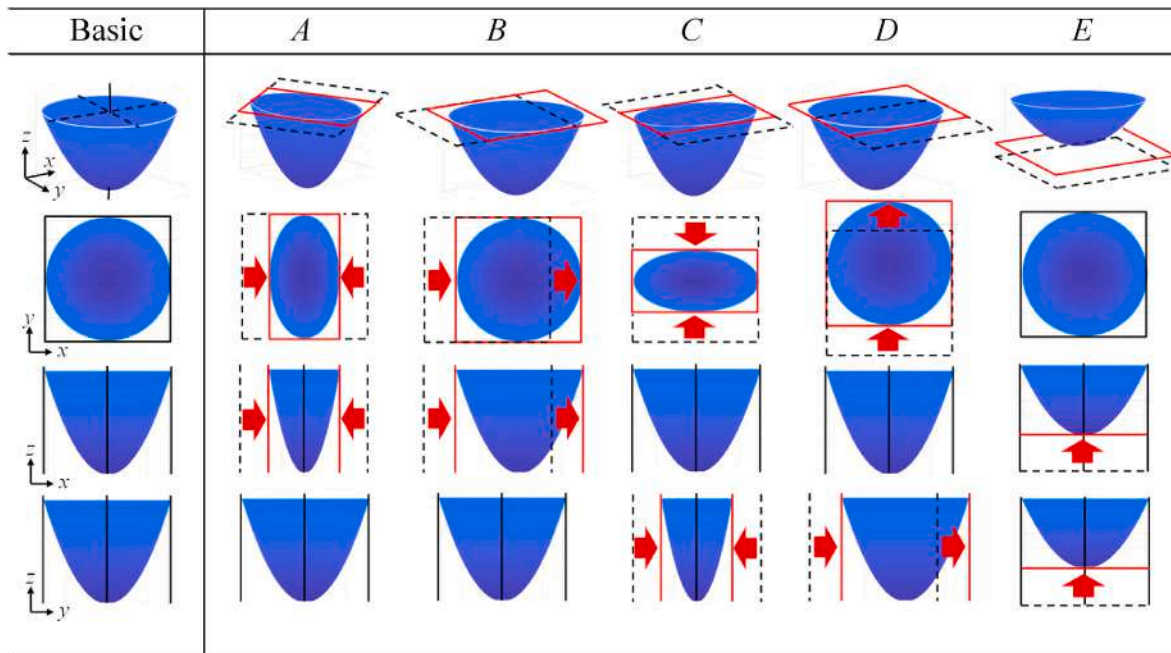

Fig. 3. The basic shape of a quadratic surface and typical shape changes obtained by varying the value of each coefficient of the quadratic surface function.
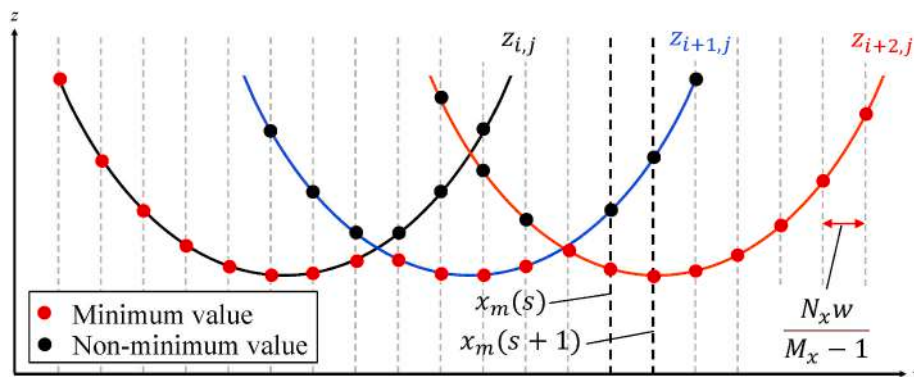

Fig. 4. Schematic for applying point cloud data to achieve continuous connection of quadratic function surfaces by selecting the minimum value of z.

Fig. 5(a) and Table 1 show the basic quadratic surface array created by the developed program before adding randomness and the value of each configuration variable, respectively. The width, depth and the number of quadratic surfaces were as set, and the program was confirmed to work properly. The RSS created by randomizing the size of these basic quadratic surface arrays is shown in Fig. 5(b). The randomness of the size was achieved by generating random values in the dynamic range 0.25–1.0 at the coefficients A and C in Equation (2). In this case, the relationship between the randomness of the size and the random value is expressed by the following equation.

$$w_{max} = \frac{w}{\sqrt{rand_{min}}} \qquad (6\text{-a})$$

$$w_{min} = \frac{w}{\sqrt{rand_{max}}} \qquad (6\text{-b})$$

where w_{max}, w_{min}, $rand_{max}$ and $rand_{min}$ are maximum and minimum values for the size variation range of a quadratic surface and the dy-
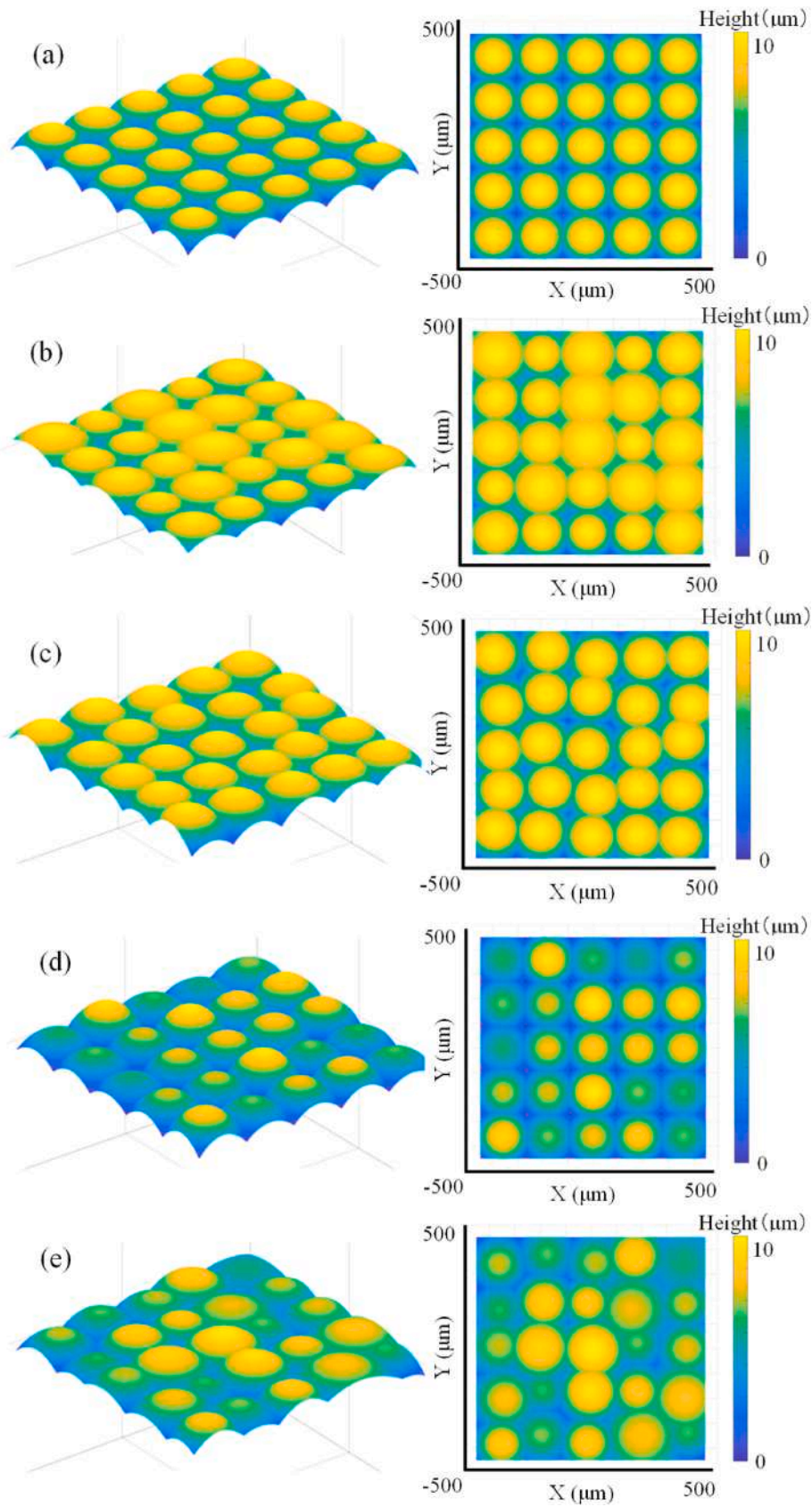
Fig. 5. Surfaces created by using the proposed design method: (a) basic quadratic surface array; RSSs with randomized (b) size, (c) position, (d) depth, and (e) combination of size, position and depth.

Table 1
RSS design parameters.

Design parameters	Value
Basic dimple width w (μm)	180
Basic dimple depth d (μm)	10
Number of dimples on X-axis N_x	5
Number of dimples on Y-axis N_y	5
Number of meshes on X-axis M_y	1000
Number of meshes on Y-axis M_y	1000

namic range of random values.

In the same way, position-only and depth-only randomized RSSs were created by generating random numbers in the dynamic range −25 to 25 at coefficients B and D, and 0.6 to 1.0 at coefficient E in Equation (2), respectively, as shown in Fig. 5(c) and (d). The dynamic ranges of position and depth generated by random values are defined by the following equations.

$$p_{max} = rand_{max} \tag{7-a}$$

$$p_{min} = rand_{min} \tag{7-b}$$

$$d_{max} = rand_{max}d \tag{8-a}$$

$$d_{min} = rand_{min}d \tag{8-b}$$

where p_{max}, p_{min}, d_{max} and d_{min} are maximum and minimum values for the position and depth variation range of a quadratic surface. Each of the randomness of quadratic surfaces can be freely combined as the example in Fig. 5(e), which was randomized in size, position, and depth by generating random values at every coefficient in Equation (2). These RSS in Fig. 5 showed a wide variety of RSS design possibilities by this method.

In addition, the proposed RSS design method allows for the control of randomness by adjusting the random value range, as shown in Fig. 6. The minimum value for the dynamic range of random values was halved to 0.5, 0.25, and 0.125 for the RSS whose size was randomized only. Based on Equation (6), the randomness of the RSS size increased as the minimum value of the random number range decreased. The same phenomenon occurred for RSS with only randomized positions and depths, and even for RSS with a combination of these randomness. These design results show that it is possible to control the randomness of RSS by adjusting the random value range.

2.3. Tool path generation method

Tool path generation was performed to command the tool motion for ultra-precision cutting of the designed RSS by diamond turning. A tool
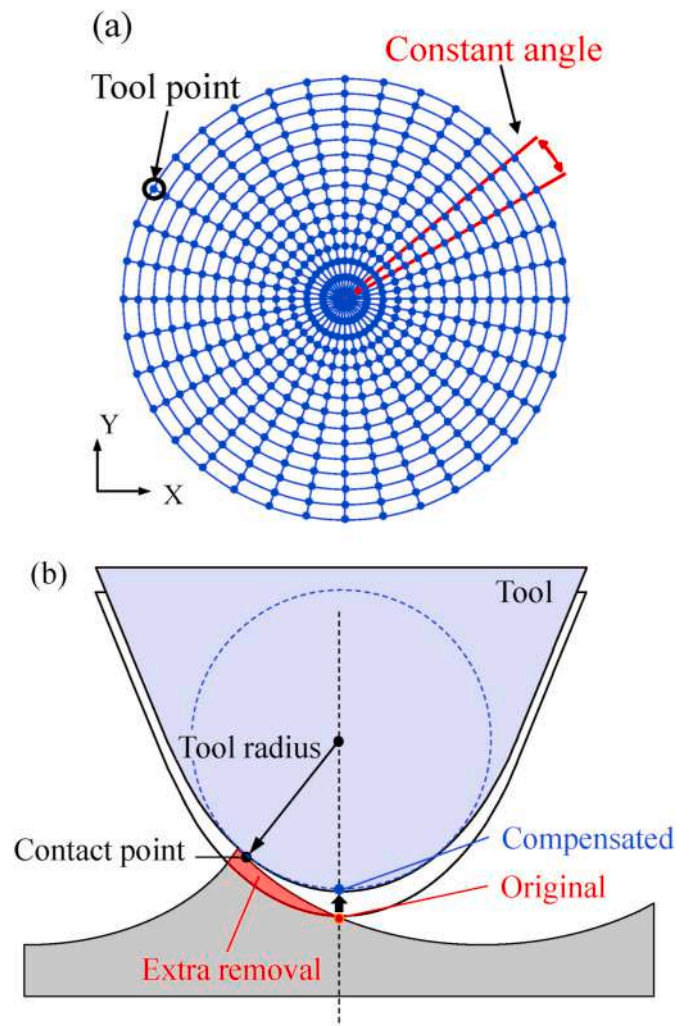

Fig. 7. (a) Point cloud data of tool path programs arranged by the isometric method; (b) schematic of tool radius compensation for each point cloud data.
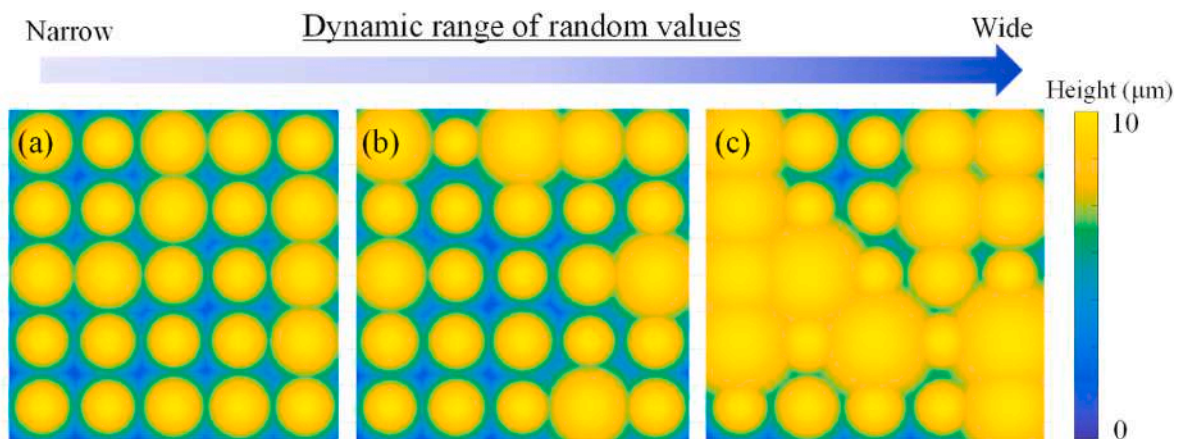

Fig. 6. A dimple array randomized only in size, created by gradually widening the dynamic range of random values from (a) 0.5 to 1.0, (b) 0.25 to 1.0, and (c) 0.125 to 1.0.

path program consisting of point clouds data arranged by the isometric method, as shown in Fig. 7(a), is effective for machining intricate surfaces such as freeform lenses [29,30]. Cutting of the designed surface is realized by moving the tool according to the depth at each coordinate of the tool path program and the shape interpolated by spline interpolation. Simply moving the tip of the tool according to the coordinates of the designed surface results in extra removal of material, which reduces the form accuracy of the workpiece [31,32], as shown in Fig. 7(b). Therefore, in this study, the depth of cut at each coordinate was determined by using the tool radius compensation method [33], where the depth of cut was modified according to the tool radius to make the tool edge profile tangential to the ideal surface profile for preventing overcut.

2.4. Segment cutting method for interpolation error elimination

While the tool path generation based on isometric control point distribution is suitable for machining complex geometries with discontinuous profiles, such as microlens array, an interpolation error may take place and lead to distortion of dimple edges [32,34]. An interpolation error is the difference between the interpolated shape in the point cloud of the tool path program and the designed shape. For optical elements, edge distortion leads to functional degradation, such as reduced light transmission and intensity. Therefore, it is necessary to take countermeasures against the edge distortion in machining of RSS. To solve this problem, the segment cutting method was proposed by Mukaida and Yan in slow tool servo (STS) diamond turning [34]. By dividing the dimples into separate groups and cutting the dimples group by group, the generation of sharp edges becomes possible by using a continuous tool path, as shown in Fig. 8. The proposed segment cutting has also been shown to be effective in forming sharp edges in other study [35]. In order to achieve sharp dimple edges, this study utilized the segmented cutting method in FTS-based diamond turning of RSS.

As shown in Fig. 9(a), each randomized quadratic function surface of the designed RSS was arranged in a square matrix. To partition the designed surface, i and j in Equation (3), which represent the numbers of quadratic surfaces in the X- and Y-axes, were added together. The quadratic surfaces were then arranged in two groups: Group 1 where $i +$

j was an even number, and Group 2 where $i + j$ was an odd number. The partitioning of the designed RSS was done by reconnecting the quadratic surfaces corresponding to each group as in the RSS design process, as shown in Fig. 9(b). The segmented surfaces were machined sequentially to reproduce the original designed surface. In this study, to create an RSS with controllable randomness by ultra-precision cutting using FTS, both continuous and segment cutting experiments were conducted, and the results were compared to determine their effects on dimple edge distortion.

3. Experimental procedures

3.1. Surface design and tool path generation

Using the method described in Section 2.2, an RSS was designed. Fig. 10(a) illustrates the designed RSS for applications as polymer optical diffusers, which was constituted by 576 (24 × 24) convex quadratic surfaces in total. The size and height of basic quadratic surface of the dimples were 100 μm and 5 μm, respectively. Randomness was added to the size and depth of each quadratic surface by substituting a random value ranging from 0.45 to 1 for shape parameters A and C, and 0.6 to 1 for E, in Equation (2). Therefore, the size and depth of each quadratic surface vary randomly in the range of 100 μm–150 μm and 3 μm–5 μm, respectively. Fig. 10(b) shows the reverse topography of the same RSS in Fig. 10 (a), which is composed of concave dimples and can be used as a mold for molding/imprinting the designed polymer RSS shown in Fig. 10 (a). In the subsequent cutting process, Fig. 10(b) was used as both the ideal surface for machining and the reference surface for evaluating the machined mold surface. The setting parameters of the designed RSS in Fig. 10 (b) are summarized in Table 2.

For creating the designed surface in Fig. 10(b) by segment cutting, the dimples were divided into two groups based on the method described in section 2.4 (Fig. 9). The tool path for creating each group of dimples constructs a virtual surface, as shown in Fig. 11. The virtual surface shown in Fig. 11(a) is a 3D presentation of the tool path for creating dimples of Group 1 (dimple areas and cross sections indicated by blue color in Fig. 9); the virtual surface in Fig. 11(b) is a 3D presentation of the tool path for creating dimples of Group 2 (dimple areas
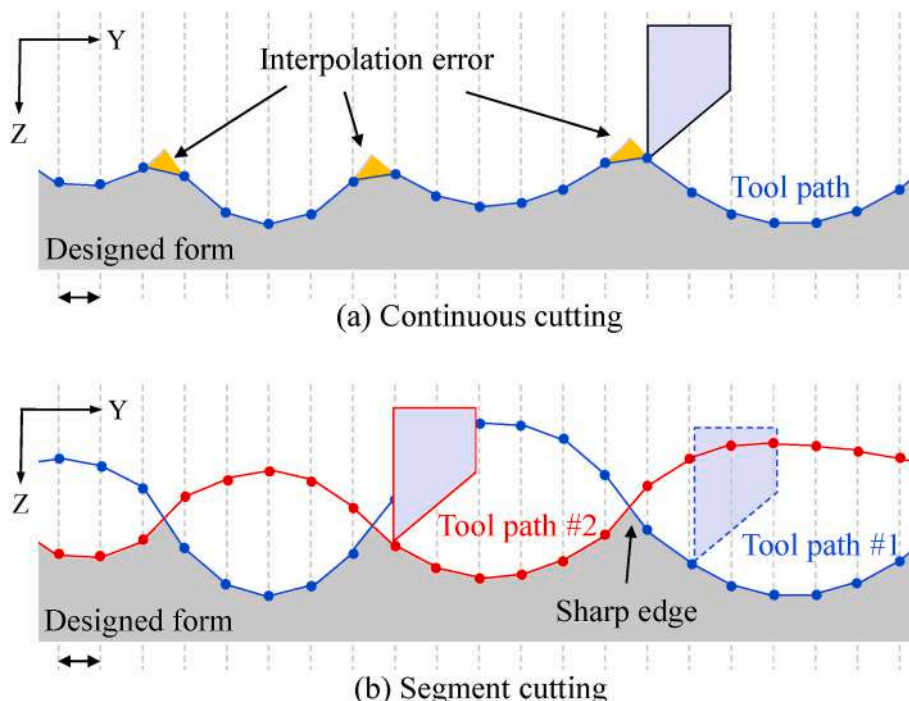

Fig. 8. (a) Schematic of form error generation due to interpolation errors in continuous cutting; (b) segment cutting for generating sharp edges.
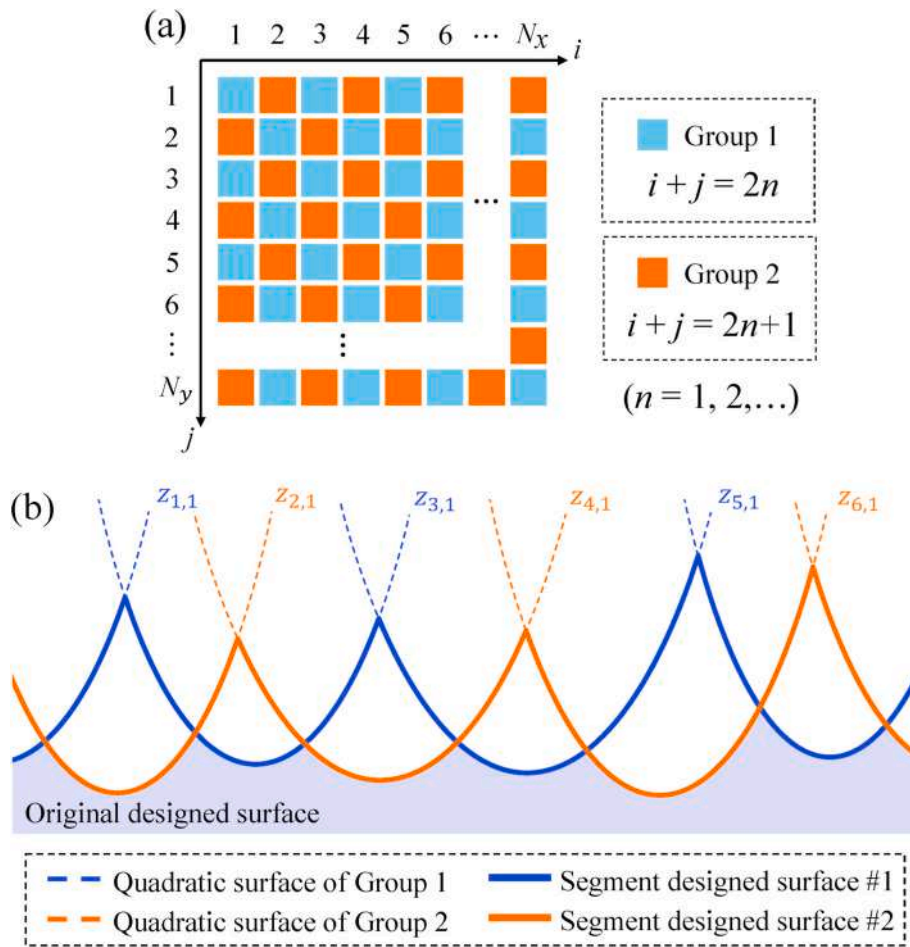
Fig. 9. (a) Partitioning of dimples into groups for segmented cutting; (b) schematic of surface stitching for tool path generation.
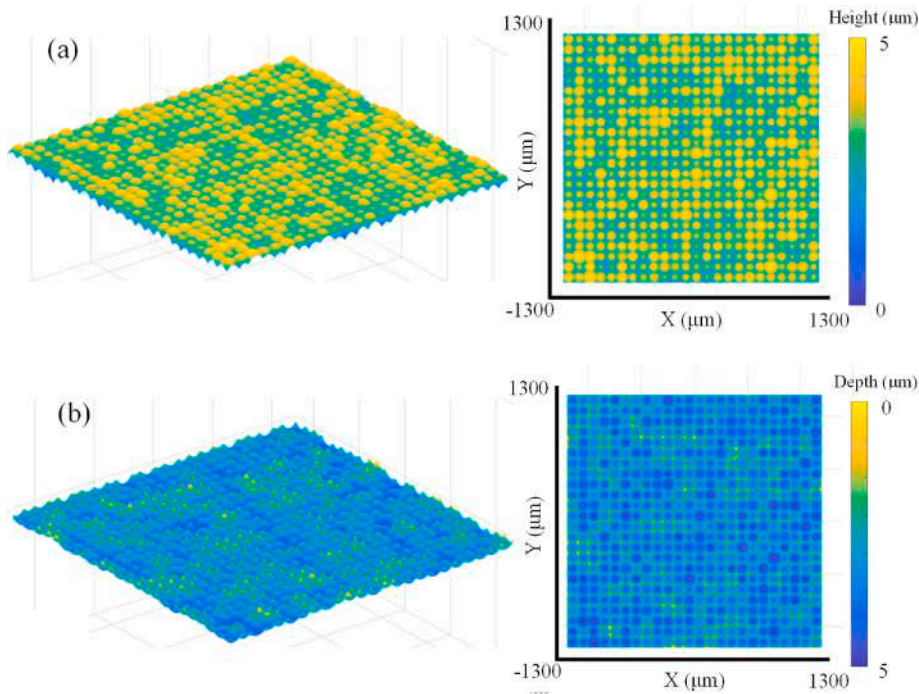

Fig. 10. (a) RSS and (b) its molds surface designed by using proposed design method for cutting experiments.

Table 2
Parameters of designed RSS for cutting experiment.

Design parameters	Value
Basic dimple width w (μm)	100
Basic dimple depth d (μm)	5
Number of dimples on X-axis N_x	24
Number of dimples on Y-axis N_y	24
Number of meshes on X-axis M_y	1000
Number of meshes on Y-axis M_y	1000
Dynamic range of random value for Coef. A and C	0.45–1.00
Dynamic range of random value for Coef. E	0.60–1.00

and cross sections indicated by orange color in Fig. 9). The two virtual surfaces in Fig. 11 intersect with each other, constructing the designed surface in Fig. 10(b). Comparing with the designed surface in Fig. 10(b), the two virtual surfaces in Fig. 11 have larger dimple size and depth. This is because the openings of the virtual surfaces are larger than those of the intersected surface on the workpiece, as seen in Fig. 9(b). However, by fitting the cutting depth value to the original design surface, same dimple size of the original design surface can be machined in segmented cutting. By enlarging the same area (the upper right corner) of both virtual surfaces in Fig. 11 (a) and (b), it was confirmed that the adjacent quadratic surfaces were properly segmented from each other.

Based on the virtual surfaces shown in Fig. 11, tool path programs were created with tool radius compensation. The created tool path programs consist of point clouds arranged at an equal interval of 1.0 μm

and an equal angle of 0.5 °.

3.2. Cutting experiment

To fabricate the designed RSS, diamond turning was performed by using a fast tool servo FTS-5000 (AMETEK Precitech Inc.), equipped on an ultraprecision lathe Nanoform X (AMETEK Precitech Inc.), as shown in Fig. 12. The FTS control system detects the coordinates of the X, C, and Z axes of the Nanofoam X in real time, and cutting was performed by moving the W axis in accordance with the tool path program for those coordinates. Compared with a slow tool servo where the entire machine tables are reciprocated, only the diamond tool is reciprocated for an FTS, which improves the acceleration and speed of the movement and reduce the follow-up errors. With the aid of FTS-based diamond turning, the total cutting time is significantly reduced compared with an STS system. The FTS unit used in this study has a maximum frequency of ~440 Hz and a maximum stroke of ~5.0 mm.

A round-nosed single-crystal diamond tool with a nose radius of 0.09 mm, a rake angle of 0°, and a clearance angle of 17° was used in the experiment. The selection of tool radius and clearance angle was made by considering the minimum width and maximum tilt angle of all quadratic surfaces in the designed RSS. An oxygen-free copper cylinder with a diameter of 20 mm was used as workpiece. In consideration of the tool radius and clearance angle, the maximum depth of cut was set to ~3.0 μm. Three cuts, two rough cut and a fine cut at depths of cut of 3.0 μm and 1.0 μm were made for finishing the designed surface. To facilitate comparative observations of the random structures, the feed rate
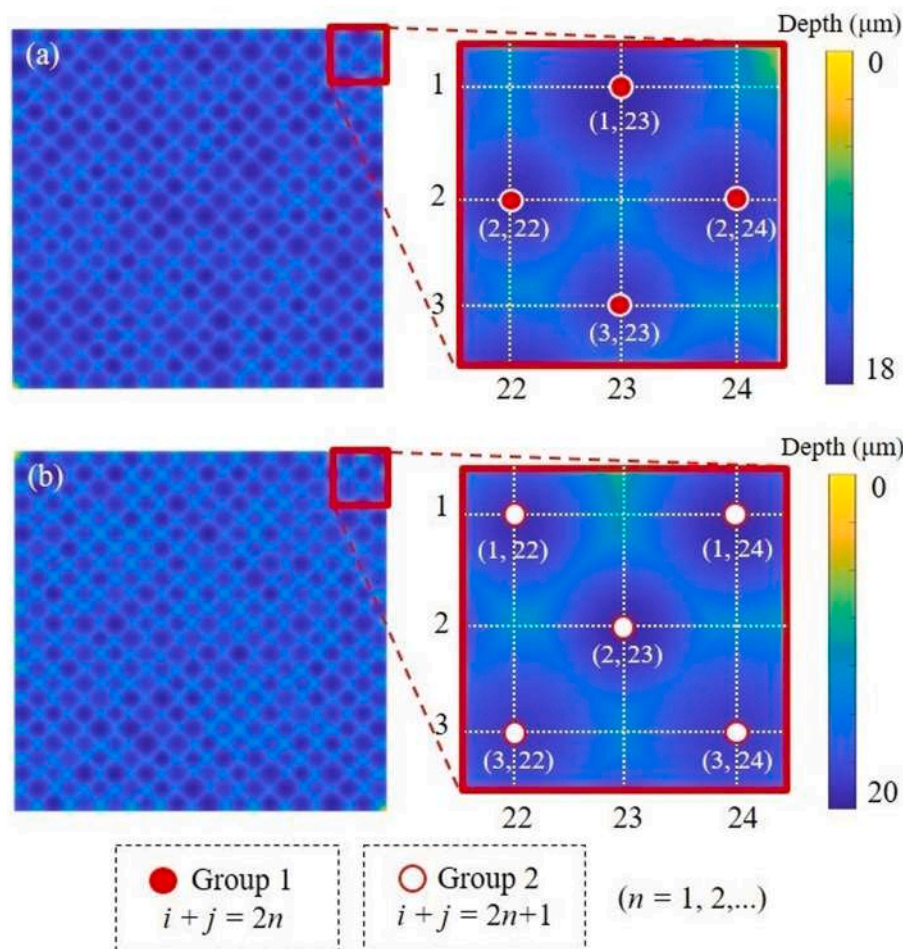
Fig. 11. Segmented designed surface for creating dimples: (a) Group 1 (dimple areas and cross sections indicated by blue color in Fig. 9) and (b) Group 2 (dimple areas and cross sections indicated by orange color in Fig. 9) with comparison of a magnified view at the same area (upper right corner). (For interpretation of the references to color in this figure legend, the reader is referred to the Web version of this article.)
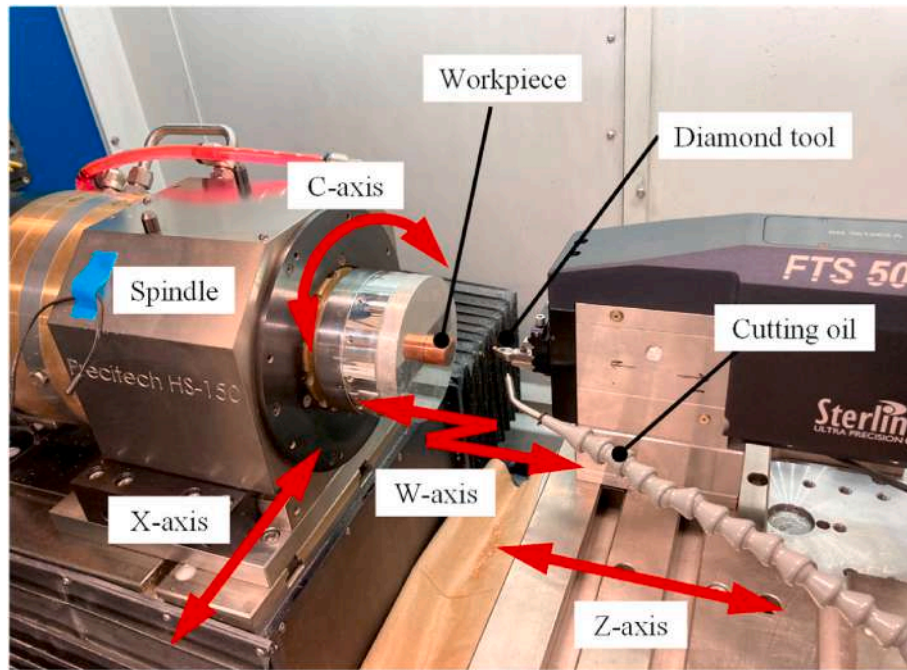
Fig. 12. Photograph of the main section of experimental setup of FTS-based diamond turning.

was set to 5 μm/rev, which is larger than the usual resolution of naked eyes. The cutting parameters are summarized in Table 3. After machining, a digital microscope VHX1000 (KEYENCE Co., Ltd.) and a white-light interferometer Talysurf CCI1000 (AMETEK Co., Ltd.) were used to observe and measure the finished surface of RSS.

4. Results and discussion

4.1. Surface topography in continuous cutting

Fig. 13(a) shows a photograph of the machined RSS by continuous cutting. It can be observed that random scattering of nature light occurred as spots with different brightness. Fig. 13(b) shows a digital microscope image of the RSS. It is clearly seen that the machined RSS is composed of various micro dimples with different size. Comparing the machined surface (Fig. 13(b)) with the designed surface (Fig. 13(c)), it can be found that the shape of the designed surface has been reproduced. For more detailed measurements, topography of the machined RSS was measured by using a white interferometer. Fig. 13(d) shows the measured topography of the machined RSS, and Fig. 13(e) shows the error map created by fitting the measured topography to the designed surface topography. From Fig. 13 (d) and (e), it can be found that the size, depth and edge position of each quadratic surface matched well

Table 3
Cutting conditions.

Cutting Parameters	Value
Depth of cut (μm)	Rough: 3
	Fine: 1
Spindle rotation rate (rpm)	100
Feed per revolution (μm/rev)	5
Cutting tool	
Tool material	Single-crystal diamond
Nose radius (mm)	0.09
Rake angle ( )	0
Clearance angle ( )	17
Workpiece	
Material	Oxygen-free copper
Diameter (mm)	6
Cutting area diameter (mm)	2.4

with the designed surface. The peak-valley (PV) and RMS values of the form error were 425 nm and 52 nm, respectively, which indicates that high-precision machining of the designed RSS was achieved in this experiment. This result validates that the randomness of RSS can be controlled by the proposed design method and the fabrication of high-precision RSS can be realized by FTS-based diamond turning.

4.2. Interpolation error-induced edge distortion

Fig. 14 shows two topography images of the machined RSS at the workpiece center and an outer area (0.9 mm from the center). Sharp edges were formed among the dimples near the workpiece center (Fig. 14(a)), while distorted edges were formed in the outer area (Fig. 14 (b)). The cause of edge distortion was the interpolation errors in the tool path program. As shown in Fig. 15, the tool path program was defined by individual cutting points placed by a constant angle of workpiece rotation. The equiangular arrangement of the cutting points results in a dense arrangement of cutting points in the center area and a sparse one in the outer area. Between the cutting points, cutting is performed at a tool position determined by interpolation based on neighboring cutting points. The interpolation error, which is the difference between the designed curve and linearly interpolated curve, depends on the density of cutting points and the discontinuity of the designed surface. In the outer area, cutting points are sparse, causing a bigger interpolation error, which distorts the edges of the machined RSS.

Simulation was done to predict the interpolation error based on the tool path program and was compared with experimental results. Fig. 16 (a) shows a map of interpolation error created by calculating the difference between the interpolated surface and the designed surface. The value of the interpolation error depends on the direction of the dimple edge and cutting direction. In the case of the edge direction is parallel to the cutting direction, the interpolation error is small and edge distortion is less likely to occur, while for the case of the direction is perpendicular to cutting direction, edge distortion is more likely to occur. These features of the interpolation error can clearly be seen in the error map. In the area shown in Fig. 16(b), the dimple edge and cutting direction intersect diagonally, resulting in an interpolation error at the overall edge. In contrast, in the area shown in Fig. 16(c), a large interpolation error occurs at the point where the dimple edge and cutting direction
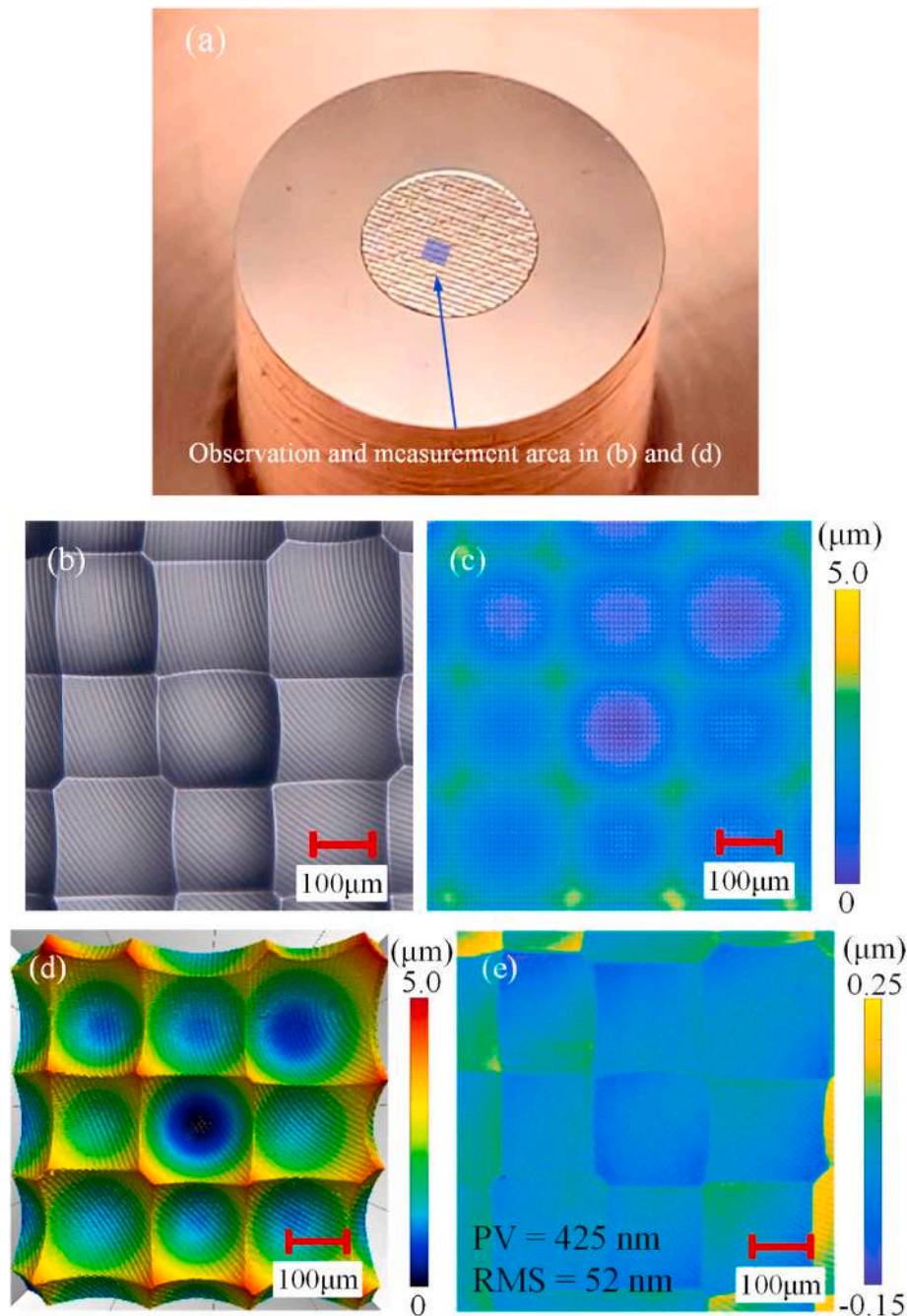
Fig. 13. Observation and measurement results of a machined RSS: (a) optical image; (b) enlarged view by laser microscope; (c) designed surface topography; (d) measured topography by white light interferometer; (e) error map created by comparing Fig. 12(c) and (d).

intersect perpendicularly, whereas no obvious interpolation error can be identified at the point where the dimple edge and cutting direction intersect parallelly. Fig. 16(d) and (e) show comparison of an error map and a microscope image of the machined surface. It can be confirmed that the location of the edge distortion corresponds exactly to the interpolation error of the error map.

4.3. Surface topography in segment cutting

Segmented cutting as described in Section 2.4 was performed to prevent edge distortion. Fig. 17 shows a comparison of surface topography obtained by the continuous and segment cutting, respectively, in the same outer area of the workpiece. Although the size, depth, and edge direction of the dimples in the two methods are generally consistent, the

edge distortions that occurred in continuous cutting were improved significantly in segmented cutting. The segment cutting could compensate the interpolation error and generate sharp edges close to the designed surface.

In order to quantitatively verify the improvement of edge distortion by segmented cutting, the edge cross sections of the machined dimples by continuous and segmented cutting were measured. At the edge of the dimple in workpiece center area, as shown in Fig. 18(a) and (b), three cross-sectional profiles, namely the designed, predicted, and measured profiles, are consistent, confirming that the dimple shape was reproduced precisely. The P–V values of the edge cross-sectional error of the center area for continuous and segmented cutting are 68 nm and 85 nm, respectively. These results indicate that both cutting methods achieved high accuracy at the center area. However, at the outer area, the
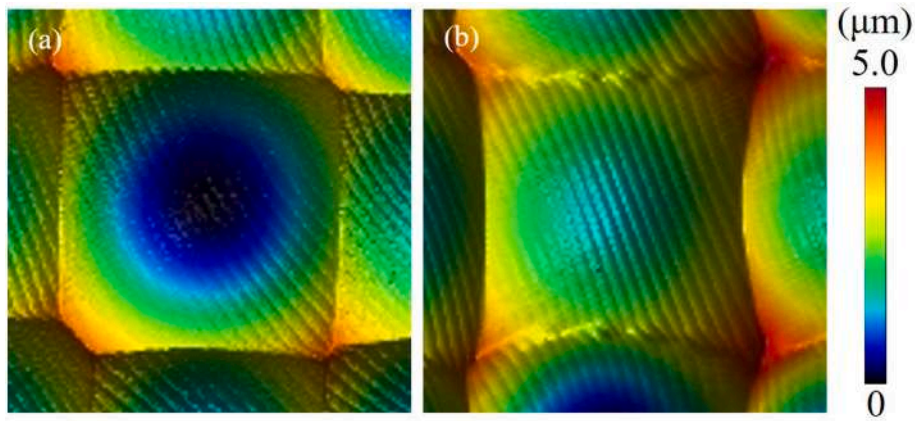
Fig. 14. Topography images of (a) workpiece center area and (b) outer area.
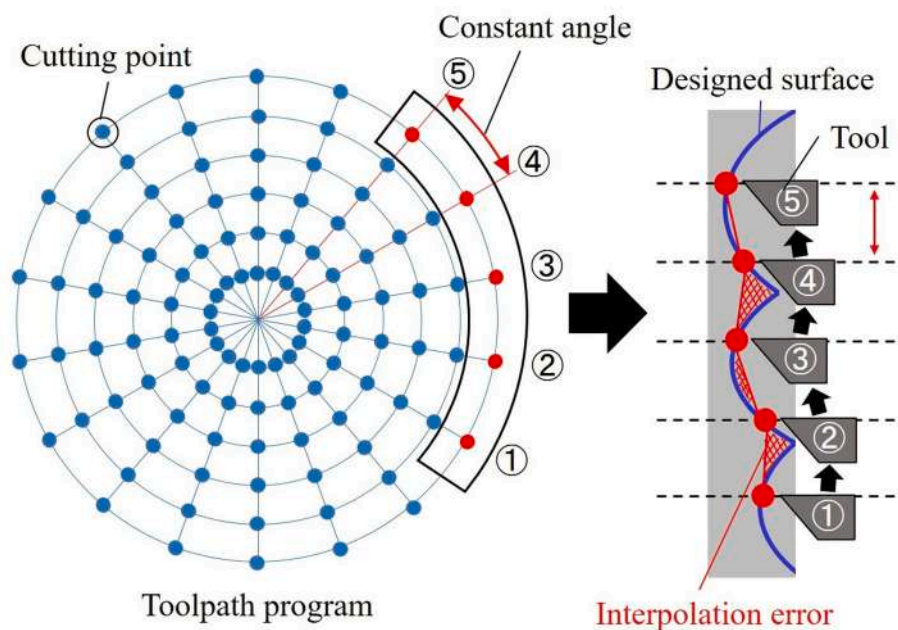

Fig. 15. Interpolation error in toolpath program generation.

designed edge profile did not match the measured one in continuous cutting, resulting in a large form error, as shown in Fig. 18(c). The P–V and RMS values of the form error between the designed shape and the measurement result were 228 nm and 149 nm, respectively. On the other hand, the P–V and RMS values of the form error between the measured and predicted edge profiles by simulation were 161 nm and 39 nm, respectively. Based on a comparison of the RMS values, it can be estimated that the ratio of the form error due to interpolation error to the total error was ~74%. This percentage indicates that the interpolation error is the major factor of edge distortion.

Edge distortion has also been reported in STS diamond turning, and machine follow-up error was considered as one of the major factors. A dimple edge is a place where the machine table motion changes, and therefore large follow-up errors are likely to occur. It is assumed that the follow-up error also affects the edge distortion in FTS-based diamond turning. However, compared with STS, the follow-up error in FTS is far smaller. Thus, the interpolation error has a larger effect on the edge distortion than the follow-up error.

On the contrary, significant improvement of edge profile was observed in the segment cutting. Fig. 17(d) shows a cross-sectional profile of a dimple edge in outer area of the workpiece machined by

segment cutting. Compared with continuous cutting, the improvement of edge profile can be confirmed in segment cutting. The P–V and RMS values of the form error were 66 nm and 42 nm, respectively, 71% and 72% lower than those of continuous cutting. It is considered that the form error caused by the interpolation of the tool path program, which was a major cause of edge distortion, was greatly reduced by segmented cutting. Therefore, segmented cutting is an effective machining method for RSS with controllable randomness.

5. Conclusions

New design and fabrication methods for RSS with controllable randomness by using FTS-based diamond turning were proposed and their effectiveness were verified by experiments. The main conclusions are summarized below:

(1) An RSS design method was developed by utilizing quadratic function surfaces and random numbers. Mesh structure was used to create a surface by comparing the point cloud data of each quadratic surface. The randomness of the size, position, and
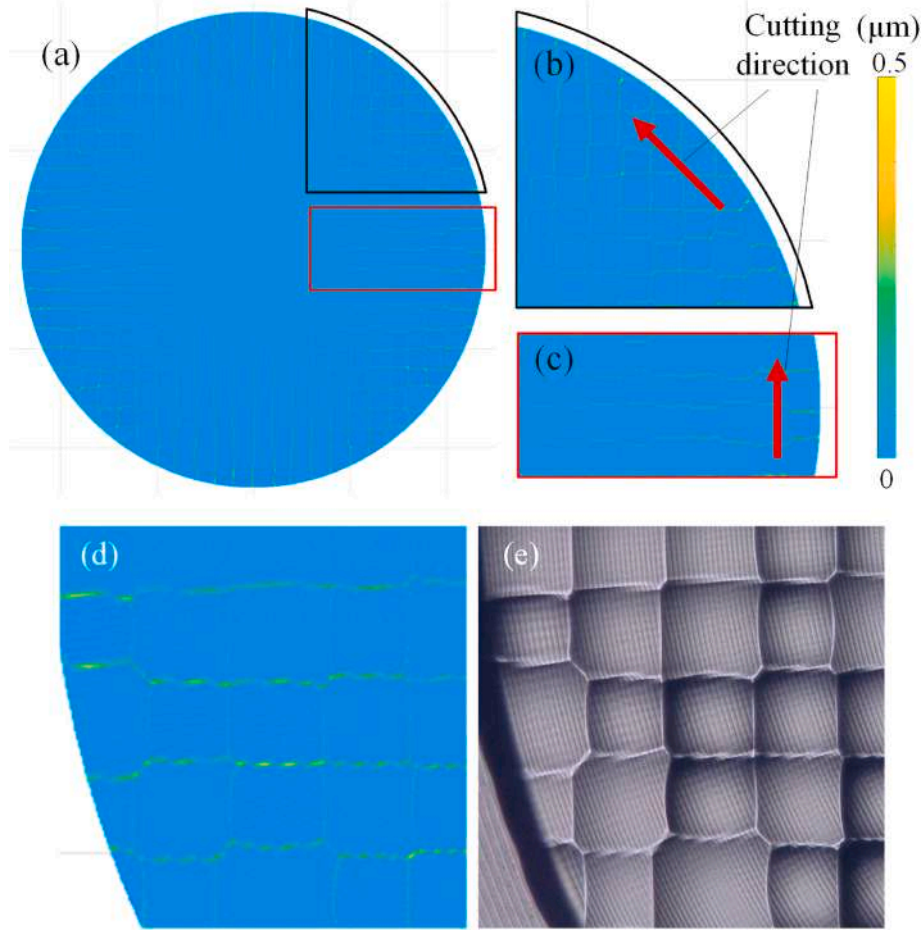
Fig. 16. Simulated interpolation error map and comparison with experimental result: (a) simulated error map; enlarged views of locations where the cutting direction and dimple edge direction cross (b) diagonally and (c) vertically/parallelly; comparison of (d) simulated error map with (e) microscope image of a machined surface at the same area.
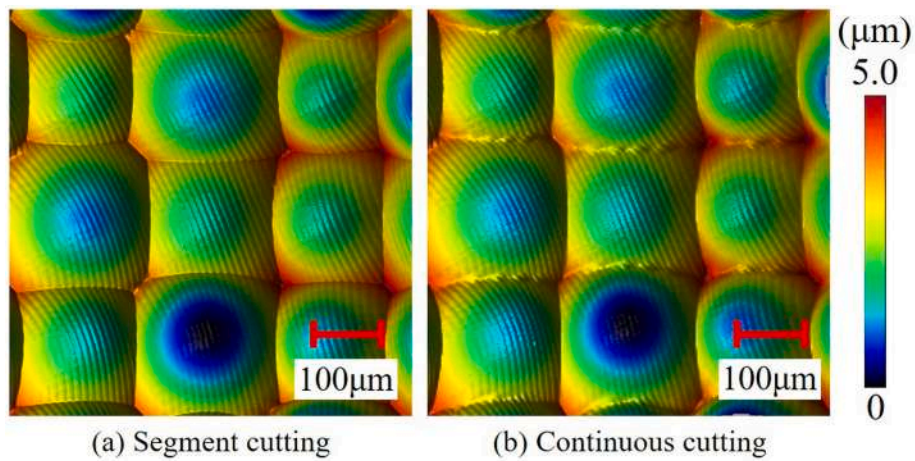

Fig. 17. Comparison of machined surfaces in the same outer area by (a) segment and (b) continuous cutting.

depth of each quadratic surface can be controlled by adjusting the dynamic range of random values.

(2) The designed RSS was fabricated by FTS-based diamond turning. The measurement of the machined surface confirmed that the size, depth, and edge position of each quadratic surface matched precisely with those in the designed surface.

(3) In continuous cutting of RSS, sharp edges were only formed near the center of the workpiece, while edge distortion was observed on the outer area. The edge distortion was mainly caused by the interpolation errors in the toolpath program created by the isometric method.
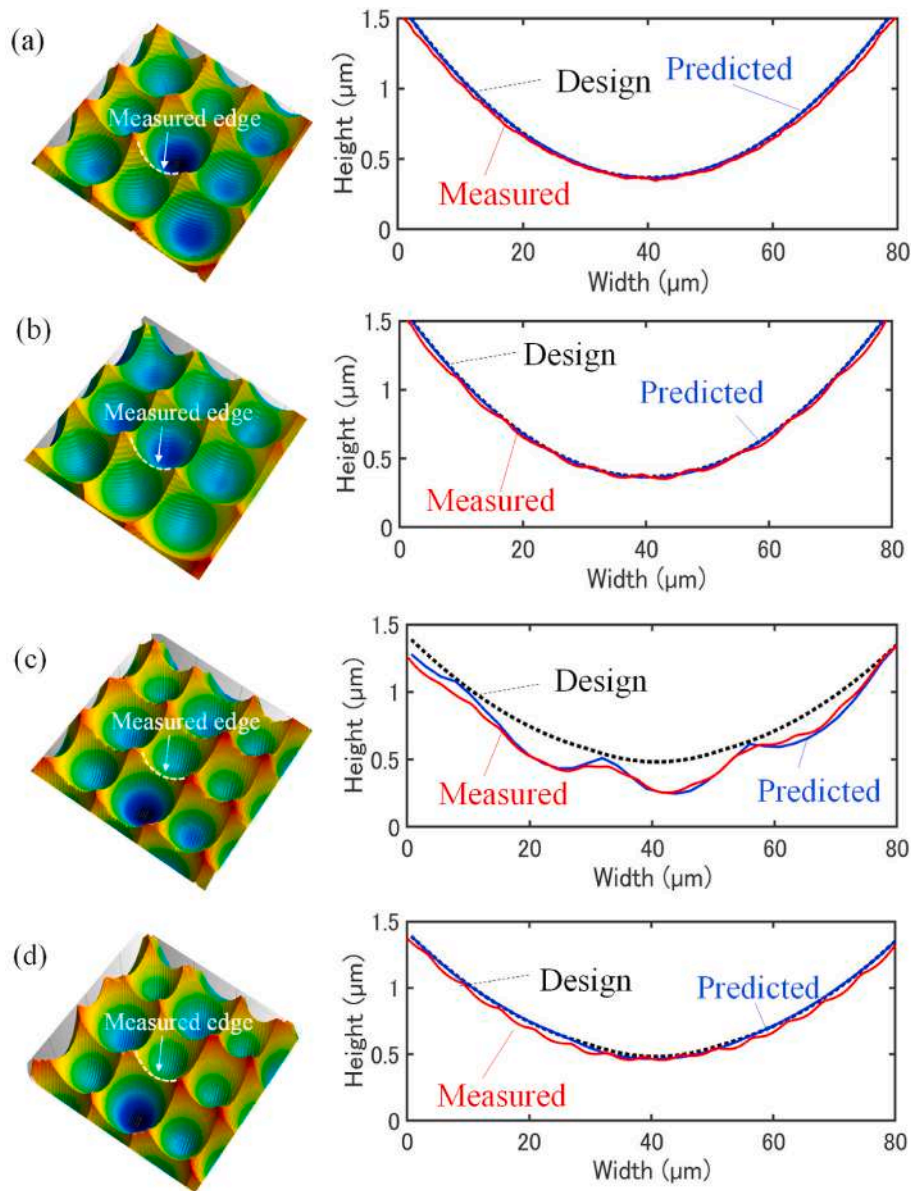
Fig. 18. Comparison of edge cross-sectional profiles: center area edge generated by (a) continuous and (b) segment cutting, and outer area edge generated by (c) continuous and (d) segment cutting.

(4) Simulation was performed to predict the form error due to interpolation error. The predicted results were consistent with the experimental results.

(5) The RSS fabricated by segmented cutting showed higher machining accuracy than continuous cutting. The edge distortion problem observed in continuous cutting was solved by segment cutting. The form error was controlled below 10 nm level PV.

This study demonstrates that FTS-based diamond turning is an effective method to fabricate RSS with controllable randomness. The results of this research showed the possibility for high-precision patterning of mold inserts for molding/imprinting processes of polymer RSS components in the optical industry and so on. The optimal design and fabrication of optical diffusers by using the proposed method and the evaluation of their optical performance will be conducted in our future research.

Declaration of competing interest

The authors declare that they have no known competing financial interests or personal relationships that could have appeared to influence the work reported in this paper.

References

[1] Hanaor DAH, Gan Y, Einav I. Static friction at fractal interfaces. Tribol Int 2016;93: 229–38. https://doi.org/10.1016/j.triboint.2015.09.016.

[2] Yong Q, Chang J, Liu Q, Jiang F, Wei D, Li H. Matt polyurethane coating: correlation of surface roughness on measurement length and gloss. Polymers 2020; 12(2). https://doi.org/10.3390/polym12020326.

[3] Yan YY, Gao N, Barthlott W. Mimicking natural superhydrophobic surfaces and grasping the wetting process: a review on recent progress in preparing superhydrophobic surfaces. Adv Colloid Interface Sci 2011;169(2):80–105. https://doi.org/10.1016/j.cis.2011.08.005.

[4] Okulova N, Johansen P, Christensen L, Taboryski R. Effect of structure hierarchy for superhydrophobic polymer surfaces studied by droplet evaporation. Nanomaterials 2018;8:10. https://doi.org/10.3390/nano8100831.

[5] Dong C, et al. Fabrication of superhydrophobic Cu surfaces with tunable regular micro and random nano-scale structures by hybrid laser texture and chemical etching. J Mater Process Technol 2011;211(7):1234–40. https://doi.org/10.1016/j.jmatprotec.2011.02.007.

[6] Dai X, et al. Hydrophilic directional slippery rough surfaces for water harvesting. Sci. Adv. 2018;4(3):1–11. https://doi.org/10.1126/sciadv.aaq0919.

[7] Zhou C, Cossairt O, Nayar S. Depth from diffusion. IEEE Comput Soc Conf Comput Vis Pattern Recogn 2010:1110–7. https://doi.org/10.1109/CVPR.2010.5540090.

[8] Kusama K, Ishinabe T, Katagiri B, Orui T, Shoshi S, Fujikake H. Double-layer anisotropic light diffusion films fabricated using a two-step UV curing technique. Jpn J Appl Phys 2016;55(4). https://doi.org/10.7567/JJAP.55.042601.

[9] Tsukamoto H, Nishiyama M. "Diffractive white-light diffuser with subwavelength structure," *Japanese*. J. Appl. Physics, Part 1 Regul. Pap. Short Notes Rev. Pap. 2006;45(8 B):6678–82. https://doi.org/10.1143/JJAP.45.6678.

[10] Ma SH, Chen LS, Huang WC. Effects of volume scattering diffusers on the color variation of white light LEDs. IEEE/OSA J. Disp. Technol. 2015;11(1):13–21. https://doi.org/10.1109/JDT.2014.2354434.

[11] Sales TRM. Structured microlens arrays for beam shaping. Opt Eng 2003;42(11):3084. https://doi.org/10.1117/1.1618817.

[12] Ducharme AD. Microlens diffusers for efficient laser speckle generation. Opt Express 2007;15(22):14573. https://doi.org/10.1364/oe.15.014573.

[13] Fang Z, Zhang H, Zhou X, Chen L. Design and fabrication of a controllable haze diffuser film. LED Disp. Technol. II 2012;8560:85600B. https://doi.org/10.1117/12.999850. November 2012.

[14] Guo T, Yu C, Li H, Su C, Bian Y, Liu X. Microlens array diffuser with randomly distributed structure parameters. J. Phys. Conf. Ser. 2016;680. https://doi.org/10.1088/1742-6596/680/1/012005.

[15] Pawluczyk R. "Holographic diffusers," *photopolymers appl. Hologr*. Opt. Data Storage, Opt. Sensors, Interconnects 1994;2042:156. https://doi.org/10.1117/12.166350. January 1994.

[16] Seurin J-F, et al. High-efficiency VCSEL arrays for illumination and sensing in consumer applications. Vertical-Cavity Surface-Emitting Lasers XX 2016;9766:97660D. https://doi.org/10.1117/12.2213295. March 2016.

[17] Edgar MP, Sun M-J, Gibson GM, Spalding GC, Phillips DB, Padgett MJ. Real-time 3D video utilizing a compressed sensing time-of-flight single-pixel camera. Opt. Trapp. Opt. Micromanipulation XIII 2016;9922:99221B. https://doi.org/10.1117/12.2239113. September 2016.

[18] Rubico Jay T. Dry etching for coherent refractive microlens arrays. Opt Eng 1994;33(11):3547. https://doi.org/10.1117/12.179880.

[19] Zhu TF, et al. Fabrication of diamond microlens arrays for monolithic imaging homogenizer. Diam Relat Mater 2017;80:54–8. https://doi.org/10.1016/j.diamond.2017.09.017. June.

[20] Chen F, et al. Rapid fabrication of a large-area close-packed quasi-periodic microlens array on BK7 glass. Opt Lett 2014;39(3):606. https://doi.org/10.1364/ol.39.000606.

[21] Ruffieux P, Scharf T, Philipoussis I, Herzig HP, Voelkel R, Weible KJ. Two step process for the fabrication of diffraction limited concave microlens arrays. Opt Express 2008;16(24):19541. https://doi.org/10.1364/oe.16.019541.

[22] Yuan ZJ, Zhou M, Dong S. Effect of diamond tool sharpness on minimum cutting thickness and cutting surface integrity in ultraprecision machining. J Mater Process Technol 1996;62(4):327–30. https://doi.org/10.1016/S0924-0136(96)02429-6.

[23] Cuttino JF, Miller AC, Schinstock DE. Performance optimization of a fast tool servo for single-point diamond turning machines. IEEE/ASME Trans. Mechatronics 1999;4(2):169–79. https://doi.org/10.1109/3516.769543.

[24] Chen C-C, Huang C-Y, Peng W-J, Cheng Y-C, Yu Z-R, Hsu W-Y. Freeform surface machining error compensation method for ultra-precision slow tool servo diamond turning. Opt. Manuf. Test. X 2013;8838(20):88380Y. https://doi.org/10.1117/12.2022981.

[25] Liu Q, Zhou X, Xu P. A new tool path for optical freeform surface fast tool servo diamond turning. Proc Inst Mech Eng Part B J Eng Manuf 2014;228(12):1721–6. https://doi.org/10.1177/0954405414523595.

[26] Yuan J, Lyu B, Hang W, Deng Q. Review on the progress of ultra-precision machining technologies. Front Mech Eng 2017;12(2):158–80. https://doi.org/10.1007/s11465-017-0455-9.

[27] Scheiding S, et al. Diamond milling or turning for the fabrication of micro lens arrays: comparing different diamond machining technologies. Adv. Fabr. Technol. Micro/Nano Opt. Photonics IV 2011;7927(24):79270N. https://doi.org/10.1117/12.874751.

[28] Il Kim S, Choi YS, Ham YN, Park CY, Kim JM. Holographic diffuser by use of a silver halide sensitized gelatin process. Appl Opt 2003;42(14):2482. https://doi.org/10.1364/ao.42.002482.

[29] Neo DWK, Kumar AS, Rahman M. A novel surface analytical model for cutting linearization error in fast tool/slow slide servo diamond turning. Precis Eng 2014;38(4):849–60. https://doi.org/10.1016/j.precisioneng.2014.05.002.

[30] Ji S, Li J, Zhao J, Feng M, Sun C, Dai H. Ultra-precision machining of a compound sinusoidal grid surface based on slow tool servo. Materials (Basel). 2018;11:6. https://doi.org/10.3390/ma11061001.

[31] Yu DP, Wong YS, Hong GS. Optimal selection of machining parameters for fast tool servo diamond turning. Int J Adv Manuf Technol 2011;57(1–4):85–99. https://doi.org/10.1007/s00170-011-3280-z.

[32] Yu DP, Gan SW, Wong YS, Hong GS, Rahman M, Yao J. Optimized tool path generation for fast tool servo diamond turning of micro-structured surfaces. Int J Adv Manuf Technol 2012;63(9–12):1137–52. https://doi.org/10.1007/s00170-012-3964-z.

[33] Nagayama K, Yan J. Deterministic error compensation for slow tool servo-driven diamond turning of freeform surface with nanometric form accuracy. J Manuf Process 2021;64:45–57. https://doi.org/10.1016/j.jmapro.2021.01.015. March 2020.

[34] Mukaida M, Yan J. Fabrication of hexagonal microlens arrays on single-crystal silicon using the tool-servo driven segment turning method. Micromachines 2017;8:11. https://doi.org/10.3390/mi8110323.

[35] Zhang L, Naples NJ, Zhou W, Yi AY. Fabrication of infrared hexagonal microlens array by novel diamond turning method and precision glass molding. 2019.